# Comparison between Computational Fluid Dynamics and Fluid-Structure Interaction Models of an Automotive Mixed Flow Turbocharger Turbine

Noor Zafirah Abu Bakar
UTM Centre for Low Carbon Transport in Cooperation with Imperial College London, Faculty of Mechanical Engineering, Universiti Teknologi Malaysia

Muhamad Hasbullah Padzillah
UTM Centre for Low Carbon Transport in Cooperation with Imperial College London, Faculty of Mechanical Engineering, Universiti Teknologi Malaysia

https://doi.org/10.5109/7183474

# Comparison between Computational Fluid Dynamics and Fluid-Structure Interaction Models of an Automotive Mixed Flow Turbocharger Turbine

Noor Zafirah Abu Bakar[1,2], Muhamad Hasbullah Padzillah[1*]

[1]UTM Centre for Low Carbon Transport in Cooperation with Imperial College London, Faculty of Mechanical Engineering, Universiti Teknologi Malaysia, Johor Bahru, Malaysia

[2]School of Engineering, Taylor's University, 1, Jalan Taylors, 47500 Subang Jaya, Selangor, Malaysia

*Author to whom correspondence should be addressed:
E-mail: mhasbullah@utm.my

**Abstract**: The inlet flow characteristics of an automotive turbine rotor have direct influence on turbine efficiency. The objectives of this study are to compare fluid characteristics of two numerical models, a non-coupled (NC) and two-way coupled (2-WC) fluid-structure interaction simulation models at turbine rotor inlet and to assess their significance. Simulations were developed using Finite Volume Method, Finite Element Analysis and Arbitrary Lagrangian-Eulerian formulation via ANSYS. Results show that there is no significant difference between NC and 2-WC models to compute overall turbine performance but show differences of flow characteristics at tongue area and turbine blade structural performance.

Keywords: mixed flow turbine, turbocharger, fluid-structure interaction, CFD, FEA, System Coupling, engineering

## 1. Introduction

According to International Energy Agency (IEA) in its 2021 statistical report, crude oil is still the primary energy source and also the second highest carbon dioxide ($CO_2$) emissions producer after coal[1]. Studies conducted by S. Hori[2] shows that in developed countries, energy consumption is considered stable. However, for developing countries, the energy consumption indicates an increasing trend. They have been many initiatives and research being implemented to reduce the energy consumption and $CO_2$ emissions. For instance, S. Hori and T. Fujita[3] studied on the incentive mechanism to build a low-carbon society in Asia region. Besides that, the most popular alternative is using renewable energies. However, recently the concept of "Green Paradox" gains attention. This concept believes that the usage of renewable energy increases the fuel consumption and emits more harmful substances, thus does not reduce the dependency on fossil fuel[4]. T. Fujisaki[4] did evaluation on "Green Paradox" concept by creating a case study in Japan.

Road sector has the largest oil consumption share by sectors which is 49.2%[1]. Since oil is still the primary energy consumed and some drawbacks on renewable energies, thus research focusing on improving the energy efficiency of internal combustion engine vehicles are highly relevant. They have been many advanced and improved technologies implemented in automotive sectors and one of them is turbocharger. Vehicles equipped with turbocharged engines have shown rapid increase in the market share with 30% in 2019 and it was projected to increase further up to 35% in 2020[5]. Application of turbocharger provides an option to vehicle manufacturers to downsize the engines, thus provide better fuel economy and at the same time better performance compare to naturally aspirated engine. There are two types of turbocharger turbine for automotive application, radial flow turbine (RFT) and mixed-flow turbine (MFT). Due to the design requirement of RFT which has 0° blade angle, it causes the peak efficiency to be around velocity ratio of 0.7. On the other hand, the leading edge design of MFT is non-radial which the peak efficiency is shifted to lower velocity ratio, a desirable condition for turbocharger application. In addition, MFT has lower inertia thus provides better transient response.

Flow characteristics at the inlet of turbine rotor have significant effects on the flow conditions inside the turbine which subsequently affecting the turbine efficiency. Therefore, they have been numerous studies conducted related to the flow behaviors at the rotor inlet. Some studies provide detail insight on the flow characteristics at rotor inlet. Padzillah et al.[6] presented flow angle distributions which consist of absolute angle, relative angle and incidence angle along spanwise direction at MFT rotor inlet. Velocity components behaviors in spanwise, streamwise and tangential were

also presented. Morrison et al.[7] made comparison of different inlet flow angles and cone angles and their effects on turbine performance. It was found that leading edge separation was minimized when the incidence angle was negative. The turbine performance could be improved by reducing the absolute flow angle at the shroud and increasing the angle at the hub which also help in reducing flow separation at the hub. Leonard et al.[8] also did study on the effects of different variant of cone angles and inlet blade angles on MFT turbine efficiency and compared the results with RFT. The changes of the cone angles and inlet blade angles did provide some benefits in certain areas but also imposed penalties at different areas. Eventually, the authors concluded that comparing to RFT, MFT was more superior in term of low inertia that provided better transient response rather that improving efficiency.

There are studies focusing on different incoming flow conditions toward the rotor inlet. Lee et al.[9] developed five velocity profiles to study about their impact on the spanwise flow. It was concluded that velocity profile with higher axial flow produced higher flow capacity, showed reduction in incidence angle and minimized hub separation flow. Padzillah et al.[10] compared flow unsteadiness between vaned and vaneless turbines under pulsating condition. The results showed that both turbines had maximum efficiency at incidence angle range between -40° to -50° which was a significant shift from the conventional range of -20° to -30°[11]. In addition, vaneless turbine had lower absolute flow angle due to the flow inclined to move radially inward at higher span position. Morrison et al.[12] also did study related to vane which the authors made comparison between a straight baseline vane with multiple design of leaned vanes. The outcome was the most leaned vane produced the best turbine performance and reduce positive incidence angle at the hub. While most researchers conducted their studies for steady and pulsating flow, Ding et al.[13] investigated the influence of swirling inlet flow on turbine performance. It was concluded in their studies that swirl flow had major impact on the flow angles which causes an increase in turbine capacity and reduction in its efficiency.

Some research studied on the geometries of the vane and rotor itself to investigate the impact on the inlet flow conditions. Gupta et al.[14] developed a new generation of variable vane that was capable in controlling the tip leakage flow. The new design was able to achieve 2% increase in engine rated power and 7% increase for the torque. Khairuddin et al.[15] performed several combinations of optimized geometries and analyzed their effect on turbine performance. It was presented that the optimized leading edge alone did not result in any efficiency increase but when paired with optimized hub and shroud, 1% increase in efficiency was achieved. Chen et al.[16] also did design change on the leading edge of MFT by making curvature on the leading edge rather than a straight design. The new design showed that the flow was less sensitive to the incidence angle and hence, the average instantaneous turbine efficiency was improved.

The multiple studies related to the inlet flow conditions at turbine rotor proof how importance the influence of the inlet flow to the turbine performance. Even though the studies were validated with experimental data, they were conducted by considering only the fluid domain. In real condition, there are constant interactions between the fluid and the rotor structure, mainly the rotor blades. The pressure from the fluids acts on the blades, which cause the blades to deform. The deformation of the blades will then affect the flow characteristics. As per author knowledge, there is no study has yet been conducted that analyze the flow characteristics inside MFT turbine due to these fluid-structure interactions (FSI). Thus, the objectives of this paper are to provide insights on the flow characteristics at rotor inlet of MFT when the fluid is coupled with the structure, which in this study is the rotor blades and then compare the results with non-coupled simulation model. Since fully coupled FSI is computationally expensive, thus with this study it provides an indicator whether is it required or not required to include FSI for inlet flow MFT simulation.

## 2. Methodology

Two types of numerical simulation models were established which were non-coupled (NC) simulation and two-way coupled simulation (2-WC). Figure 1(a) and 1(b) display the flow diagram of NC and 2-WC numerical models respectively. Computational Fluid Dynamics (CFD) calculation using Finite Volume Method (FVM) was carried out by using ANSYS CFX 19.1 solver and Finite Element Analysis (FEA) was computed using ANSYS Mechanical Static Structural 19.1 solver. Figure 2 shows the fluid domain $\Omega_f$ which is the fluid passage, the structure domain $\Omega_s$ which is the rotor blade, and fluid-structure interface $\Gamma_{fs}$ which is the rotor blade surface. The fluid-structure interface $\Gamma_{fs}$ is defined by $\Gamma_{fs} = \Omega_f \cap \Omega_s$. The subscript $f$ and $s$ represent fluid and structure respectively. The simulation models are full 3-Dimensional (3D) steady state models and Fig. 2 shows only one portion of the domains for illustration purpose only.

NC means that it is a one-way communication from fluid domain in CFX to structure domain in Static Structural and there is no coupling between the two domains as shown in Fig. 1(a). CFX solved the fluid domain using Finite Volume Method (FVM) until the equations converged. Then, Static Structural received the final input from CFX without considering the calculation history in CFX. In NC model, static pressure acting on fluid-structure interface $\Gamma_{fs}$ was directly transferred from CFX to Static Structural. In Static Structural, the pressure loading input was converted to force to determine the deformation and stress values on the rotor blades using FEA. In CFX, it was assumed that the blades were rigid bodies.

In 2-WC model as shown in Fig. 1(b), System Coupling

(SC) was used as an interface between CFX and Static Structural as a medium of communication, thus these two solvers did not directly communicate with each other. SC employed partitioned approach which means that each solver computed their own data separately and implicitly. SC only managed the data transfer explicitly between the two solvers. Once CFX was converged, the forces data acting on fluid-structure interface $\Gamma_{fs}$ were transferred to SC then to Static Structural. The forces were interpolated on the structure mesh before they were solved for displacement and subsequently, strain and stress. The displacement data were transferred to SC before sending to CFX. Once CFX received the displacement data, the data were interpolated on fluid mesh which the fluid mesh underwent deformation. SC itself had it owns iteration number and residual value for convergence to ensure the accuracy of the transferred data. SC ensured that the transferred force and displacement data met the determined residual values or iteration numbers before it allowed for the next loop iteration.

Since SC used partitioned method, it employed conforming mesh method in treating the fluid-structure interface $\Gamma_{fs}$ [17]. In conforming mesh method, $\Gamma_{fs}$ was treated as physical boundary condition and considered as part of the solution process. Fluid domain mesh and structural domain mesh must conform with the interface because of the mesh deformation or movement. Thus, mesh updating or re-meshing was required for every iteration[17]. Arbitrary Lagrangian-Eulerian (ALE) developed by M. Souli and D.J. Benson[18] was applied in SC which in this technique, the moving mesh was included in fluid dynamic equations. Eq. 1 and 2 show the continuity equation and Navier-Stokes equation with ALE technique for 3D viscous and incompressible flow.

$$\nabla \bullet v_f = 0 \text{ on } \Omega_f \qquad (1)$$

$$\rho_f \frac{\partial v_f}{\partial t} + \rho_f \left( \left( v_f - u \right) \bullet \nabla \right) v_f = $$
$$-\nabla p + \mu \Delta v_f \text{ on } \Omega_f \qquad (2)$$

Where $v_f$ is fluid velocity fluid in m s$^{-1}$, $\rho_f$ is fluid density in kg m$^{-3}$, and $\mu$ is fluid dynamic viscosity in N s m$^{-2}$. The term $v_f - u$ is the relative velocity of fluid particle to ALE coordinate with $u$ is the mesh velocity on $\Gamma_{fs}$ in m s$^{-1}$. The first term in Eq. 2 was zero when steady state simulation was applied.

Dirichlet and Neumann conditions were applied on $\Gamma_{fs}$ as shown in Eq. 3 and 4 to keep the no-slip boundary condition on the interface.

$$\sigma_{ij}^s n_i = \sigma_{ij}^f n_i \text{ on } \Gamma_{fs} \qquad (3)$$

$$x_i^s = x_i^f \text{ on } \Gamma_{fs} \qquad (4)$$

Where $\sigma$ is the stress in N m$^{-2}$ at respective domain on $\Gamma_{fs}$, $n$ is the unit vector at $\partial\Omega_f = \Gamma_{fs}$ and $\partial\Omega_s = \Gamma_{fs}$, and $x$ is the displacement of respective domain on $\Gamma_{fs}$ in meter (m).

The governing equation for structural domain is given by Eq. 5, where $\mathbf{M}$ is the mass matrix in kg, $\mathbf{K}$ is the stiffness matrix in N m$^{-1}$ and $\mathbf{C}$ is the damping matrix in N m s$^{-1}$ with $\mathbf{F}$ is the force vector in N. The $\ddot{\mathbf{X}}$, $\dot{\mathbf{X}}$ and X are simply $\frac{\partial^2 x}{\partial t}, \frac{\partial x}{\partial t}$ and $x$ respectively.

$$\mathbf{M\ddot{X} + K\dot{X} + CX = F} \qquad (5)$$

## 2.1 Geometry

Figure 3 shows the turbocharger geometries assembly in CFX which consist of an inlet duct, a volute which is an altered Holset H3B[19], 15 blades vane with NACA 0015 profile, and a MFT rotor. The inlet and outlet are also shown in the figure. The MFT rotor was designed by
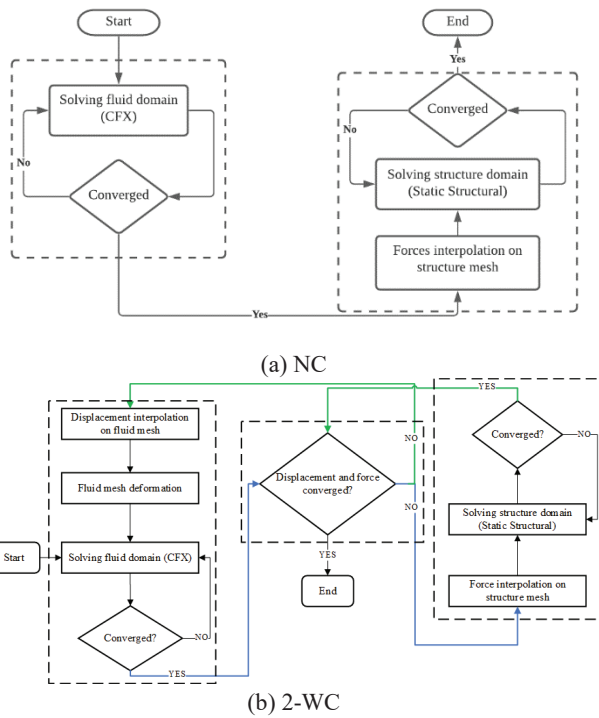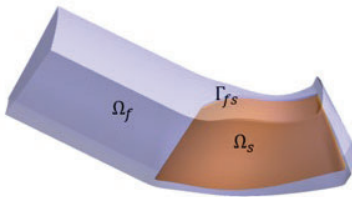


(a) NC

(b) 2-WC

**Fig. 1:** Simulation model flow diagrams



**Fig. 2:** Fluid domain $\Omega_f$, solid domain $\Omega_s$, and fluid-structure interface $\Gamma_{fs}$.

Abidat[20] and labelled as Rotor *A*. This rotor has 12 blades, constant blade angle of 20°, a cone angle of 40°, chord axial length of 40 mm, and tip gap height of 3 mm. In Static Structural, only the rotor blades with the hub were modelled as shown in Fig. 4.
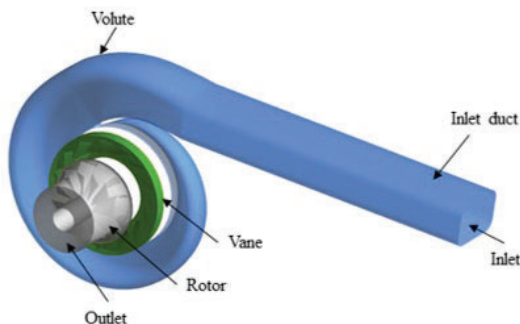


**Fig. 3:** Turbocharger geometries assembly.

## 2.2 Meshing

Since there were two individual solvers, CFX and Static Structural, the meshing procedures were implemented separately. For fluid domain, the inlet duct and volute were designed in Solidworks and the geometries were imported to Ansys ICEM for meshing. The mesh type for these geometries was unstructured hexahedral mesh. Meshing for vane and rotor were done using Ansys TurboGrid. For vane, it required three profile lines which were a hub, a shroud and an intermediate profile line for the meshing. While for rotor, it required eight profile lines because of the complexity of the shapes which were a hub, a shroud, and six intermediate profile lines. The mesh type for vane and rotor was structured hexahedral mesh. After conducted grid independence test (GIT), the finalized node numbers for each geometry are listed in Table 1. The total nodes for the whole geometry or fluid domain in CFX were 5.33 million nodes.

Table 1: Number of nodes for each geometry in CFX

| Geometry | Number of nodes |
|---|---|
| Inlet duct | 465,192 |
| Volute | 1,604,736 |
| Vane | 995,460 |
| Rotor | 2,257,944 |
| Total | 5,332,332 |

In Static Structural, multizone method was applied to generate the mesh with hexahedral type. After carried out GIT, the number of nodes of the blades and hub were 177,813 nodes.

## 2.3 Numerical Simulation Setup

In CFX setup, the speed of the rotor was set to be 30,000 rpm which was 50% of actual rotor speed. The boundary conditions at the inlet duct were mass flow rate, static temperature of 340 K and turbulent intensity of 5%. Study conducted by A. Ismaiel and S. Yoshida[21] shows that turbulence intensity has significant impact on fatigue life of wind turbine. Thus the 5% turbulent intensity was carefully assessed. Both numerical simulations were run at eight different mass flow rates. The boundary conditions at the outlet were atmospheric pressure and temperature of 298 K. The turbulence model used was two-equations $k$-$\varepsilon$ turbulence model with scalable wall function. The $y^+$ range at the rotor blades was between 1.3 to 50. Since scalable wall function was used, it ignored the nodes that had low $y^+$ and considered from the first node at the log-law region which was approximately $y^+ = 11.06$[22]. This was to ensure that the shear stress calculation was not miscalculated.

D. Palfreyman and R.F. Martinez-Botaz[23] did comparison between two simulation models, Model 1 with Model 3 and validated them with Laser Doppler Velocimetry (LDV) measurement. Model 1 used $k$-$\varepsilon$ turbulence model with wall function and Model 3 used $k$-$\varepsilon$ turbulence model with low Reynolds treatment. The number of nodes in Model 3 was five time higher than Model 1. Results showed that both models agreed well with the measured data. Thus, two-equation $k$-$\varepsilon$ turbulence model with wall treatment was viable. Several authors also employed similar turbulence model in their turbocharger simulations, for example M.H. Padzillah et al.[10] used $k$-$\varepsilon$ turbulence model in their studies on flow unsteadiness between two different vanes, P. Newton et al.[24] studied on pulsating in double entry turbine and Z.K. Omar et al.[25] employed $k$-$\varepsilon$ turbulence to analyze aerodynamic performance on rotor blade.

Frozen rotor was selected to be the interface between the rotor and the vane. S.P. Samuel et al.[26] made comparison between frozen rotor and sliding mesh interfaces. The results showed that there was no significant difference between the two interfaces.

In NC model, the blades were set as rigid bodies while in 2-WC model, the rotor mesh was set as deformable to activate SC function. Then the blades mesh motion boundary details were set as System Coupling.

In Static Structural, the blades material was AL 6082 which was similar material used during cold flow experiment[19]. Similar rotational speed of 30,000 rpm was applied and the inner diameter of the hub was selected as the fixed support as shown in Fig. 4.
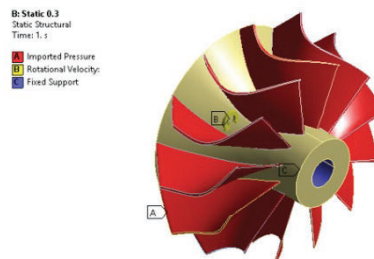


**Fig 4:** Blades and hub geometry and boundary conditions.

In NC model, pressure loading was imported from CFX. Then blade surfaces which were the fluid-structure interface $\Gamma_{fs}$ were selected to inform the solver on where the pressure loading should be imposed on. In 2-WC model, Fluid Solid Interface function was inserted and the blades were selected as the fluid-structure interface $\Gamma_{fs}$. Thus, it was very crucial to ensure that the blade geometry in CFX and Static Structural were similar in order to map both domain mesh in System Coupling.

## 3.    Results and Discussions

This section consists of four sub-sections which are the validation for the numerical models, flow analysis at rotor inlet, flow analysis at 10% streamwise of the blade and blade structural results. These analysis were carried out at 50% turbine speed (30,000 rpm) and at the most efficient point which is at pressure ratio (PR) = 1.32.

### 3.1    Numerical Models Validation
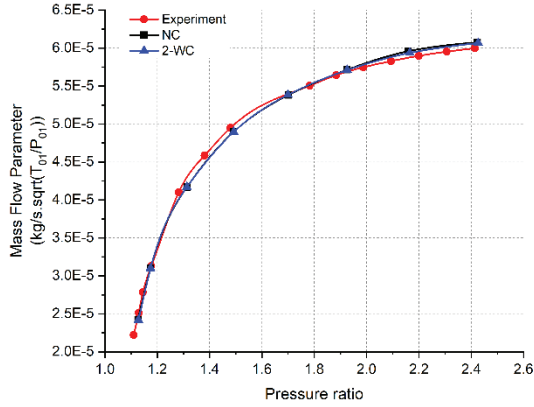


(a)    Mass Flow Parameter vs. Pressure Ratio
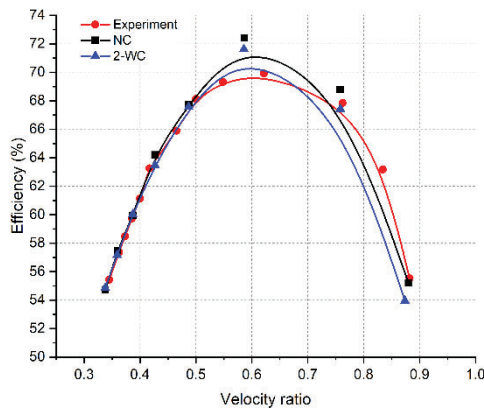


(b)    Total-to-static efficiency vs. Velocity Ratio

**Fig 5:** Comparison between NC, 2-WC and experiment data at 50% turbine speed.

Validation practices are required to ensure that the developed numerical models are viable and able to predict the trends of the measured data. Four turbine performance

parameters were extracted from the simulation models and two types of plots were generated which were mass flow parameter (MFP) against pressure ratio (PR) and total-to-static efficiency against velocity ratio (VR). MFP indicates the swallowing capacity of the turbine and reciprocally depends on the inlet pressure. The correlation between turbine efficiency and VR is very essential as the plot is used during turbine design stage, turbine matching with compressor and to indicate instantaneous efficiency for pulsating flow condition[27]. Figure 5 shows the plots of the predicted values from NC and 2-WC numerical models and are compared with cold flow test data which the detail of the experiment setup can be referred in[28]. Similar turbine performance parameters validation practices are reported by S.P. Lee et al.[9], B. Yang et al.[29], and M.H. Padzillah et al.[30].

In Fig. 5(a), both models match the trend at low PR before start to underpredict at PR 1.28 and switch to overpredict afterwards. Starting at PR 1.9, 2-WC moves closer to the experiment line. The average deviation of MFP is 1.41% for NC and 1.44% for 2-WC model.

Efficiency plot in Fig. 5(b) was harder to match with the experiment data as turbine efficiency $\eta_t$ equation is derived from several parameters as shown in Eq. 6-8. In Eq. 6, $\dot{W}_{act}$ is the actual turbine power measured in Watt (W) and $\dot{W}_{isen}$ is the isentropic turbine power. In Eq. 7, $\dot{W}_{act}$ depends on the speed of the turbine $N$ in rpm and the torque blade $\tau$ in N m. For $\dot{W}_{isen}$ in Eq. 8, it is derived from the mass flow rate $\dot{m}$ at the inlet in kg s$^{-1}$, total temperature $T_{in}$ in K and total pressure $p_{in}$ in Pa at the inlet, static pressure $p_{out}$ at the outlet, specific heat capacity $c_p$ in J kg$^{-1}$ K$^{-1}$ and ratio of specific heat γ. $c_p$ and γ were assumed constant thus might contribute to the deviation from the experimental data.

$$\eta_t = \frac{\dot{W}_{act}}{\dot{W}_{isen}} \quad (6)$$

$$\dot{W}_{act} = 2\pi N\tau \quad (7)$$

$$\dot{W}_{isen} = \dot{m}c_p T_{in}\left(1 - \left(\frac{p_{out}}{p_{in}}\right)^{\frac{\gamma}{\gamma-1}}\right) \quad (8)$$

The predicted values closely match to the experiment line at low velocity ratio until 0.50, then overpredict the trend at the maximum efficiency curve and after that, underpredict the trend. The maximum efficiency for experiment was recorded at velocity ratio 0.620 and for both models, it is at velocity ratio 0.586. The percentage different of the maximum efficiency is 3.59% for NC model and 2.43% for 2-WC model. For overall plot, the average percentage deviation is 1.38% for NC and 1.28% for 2-WC model. Since the percentage deviation are low for both plots and also the simulation models are able to

capture the trend of the experimental data, thus these simulations models are considered validated.

### 3.2 Flow Characteristics at Rotor Inlet

Figure 6 shows the comparison of NC and 2-WC models flow angles at the vane and rotor inlet at 50% span of the inlet circumference.
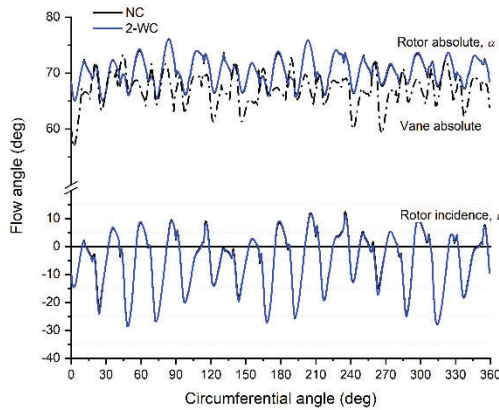


**Fig 6:** Vane and rotor inlet flow angle at circumference of 50% span.

The location of the circumferential lines around the vane and rotor inlet are displayed in Fig. 7 in red. In Figure 6, the black lines that represent NC model for rotor absolute and incidence angle are hardly visible as they are very close to 2-WC model. Similar case for the vane absolute flow angle, where the blue line represent 2-WC model is not visible. The design intent of the flow angle at vane inlet is 69° with the assumption of uniform flow exiting the volute. However, due to the geometry of vane blade and the tongue, the flow at the vane inlet is not uniform with fluctuation of ±8.25°. On the other hand, the vane serves its purpose as it able to guide the flow toward the rotor and curb the rotor inlet flow fluctuation. The fluctuation at the rotor inlet reduces to ±6°. The mean value for the vane inlet flow is 67.02° and for rotor inlet flow angle is 70.31°.

As indicated by D. Japikse[11], the optimum range of incidence angle is between -30° to -20° for radial flow turbine (RFT). The incidence angle plotted in Fig. 6 shows an upward trend compared to RFT with maximum value of 12.5° and minimum value of -28.5°. Similar trend was published by R. Morrison et al.[7]. This is due to the fact that MFT has different flow cone angle than RFT and its leading edge radius is not constant.

Even though Fig. 6 shows NC and 2-WC models are matched, the data were taken only at one location which was at circumference of 50% span. Further analysis was required to look at different locations. Thus, four spanwise lines at rotor inlet were created which are at 0° which represents position close to the tongue region, 90°, 180° and 270°. The positions of these locations are shown on the right-side of Fig. 7. The spanwise lines of 0° and 180°

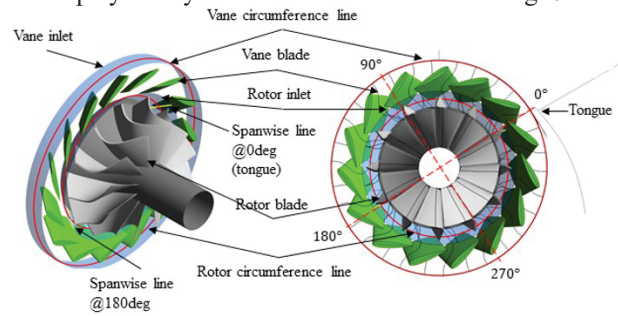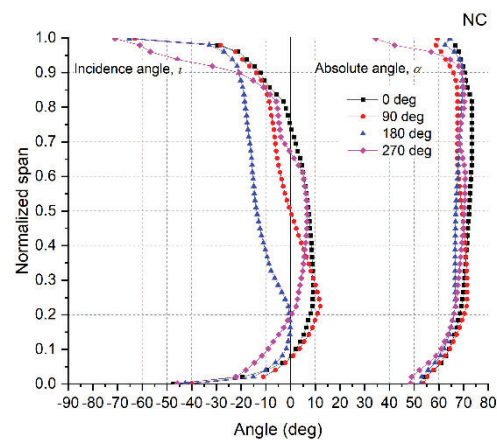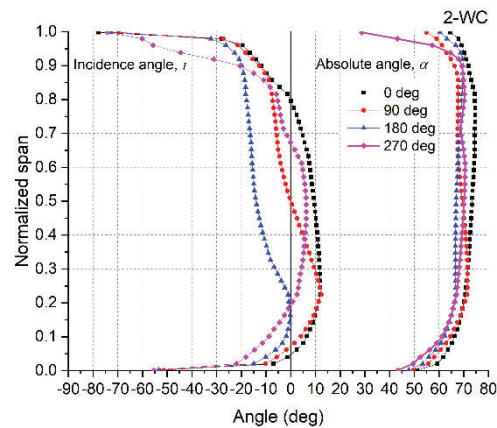are displayed as yellow line on the left side of Fig. 7.



**Fig. 7:** Location of circumference lines and spanwise lines.

The absolute flow angle $\alpha$ and incidence angles $i$ along the four spanwise lines at rotor inlet are shown in Fig.8 for both numerical models.



(a) NC model



(b) 2-WC model

**Fig. 8:** Absolute flow and incidence angles along spanwise at four circumferential location of rotor inlet

Generally, both models exhibit similar trend for all spanwise lines with some differences in the angle values which is further analyzed in the next paragraphs. Comparing in term of spanwise locations, it is observed that for absolute flow angle, the trends are almost similar among the spanwise lines. The mean absolute flow angle

at all four locations is 68.24° which is close the mean value at the 50% span circumference. The absolute angle at 180° position shows more consistent value especially between 0.2 to 0.8 span length. However, for incidence angles, there are significant differences which each spanwise line has its own line curve. But these line curves exhibit a trend which at 0° spanwise line, most of the incidence angles are located in positive region except at the high and low end of the span. This proof that the non-uniformity flow caused by the tongue has significant impact on the incidence angle. Moving to 90°, the curve is now shifted toward the negative side from 0.49 to 1.00 span length. However, from 0.08 to 0.49, it has the most positive incidence angle values. At 180°, all points in the span length are situated in negative region. This infers that the most optimum locations among the four is at 180°. At 270°, the curve is shifted back toward the positive side. Since 0° and 180° lines are at the most positive and negative sides respectively, these two positions were further analyzed for the flow angles and velocity components.
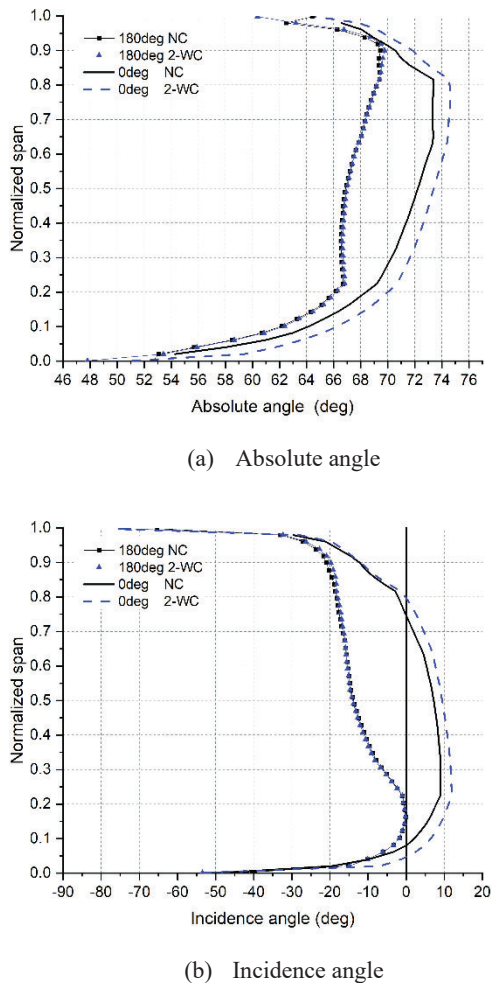
Figure 9(a) and 9(b) display the comparison of absolute and incidence angle respectively along span length at 0° and 180° circumference position for NC and 2-WC models. Both angles are almost identical at 180°. The maximum difference relative to NC model is located at the bottom of the hub with percentage difference of 43.18% and 9.18% for absolute angle and incidence angle respectively.

At 0°, 2-WC shifts toward increasing positive side. It is more obvious for the absolute angle where the whole curve is offset compares to incidence angle at which occurs between the range 0.02 to 0.86 span length. The maximum percentage different relative to NC for absolute angle is 2144.16% at 0.082 span length and for incidence angle is 102.26% at 0.16 span length.

The flow conditions were further analyzed by looking at the velocity components. As shown in Eq. 9, the relative velocity $v_{rel}$ consists of meridional velocity $v_m$ and tangential velocity $v_{tg}$ where meridional velocity $v_m$ components are spanwise velocity $v_{sp}$ and streamwise velocity $v_{st}$ as shown in Eq. 10.

$$v_{rel} = v_m + v_{tg} \qquad (9)$$

$$v_m = v_{sp} + v_{st} \qquad (10)$$



(a) Absolute angle



(b) Incidence angle

**Fig 9:** Comparison of flow angles for NC and 2-WC along span length at 0° and 180° circumferential location.
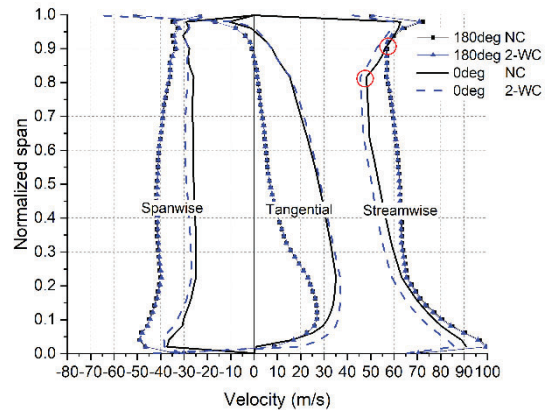


**Fig 10:** Comparison of velocity components for NC and 2-WC models along span length at 0° and 180° circumferential location

Figure 10 shows the comparison of streamwise, spanwise and tangential velocities for NC and 2-WC models along span length at 0° and 180° circumference. As expected, there is no much deviation for all three velocities at 180° for both models, whereby at 0°, there are offsets between the models.

Streamwise velocity shows the dominant component based on its magnitude. At shroud, there is a sudden drop of velocity as shown in the red circles. The drop at 0° occurs at 0.82 span length a bit later than 180° which occurs at 0.92 span length. This sudden drop is due to the tip clearance of rotor leading edge. At 0°, 2-WC model shows a consistent offset to the left by average of 6.04%

from NC model which means the streamwise velocity magnitude in 2-WC is lower.

For spanwise velocity, it can be observed that close to the shroud, the velocity shows irregular patterns which also caused by the tip clearance. Spanwise velocity falls in negative side along its span length which indicates that there is a motion of fluid from shroud to hub that slows down the meridional velocity. This is due to the different radial distance of the vane trailing edge that cause the fluid to enter the rotor at different time at shroud and hub [6]. At 0.85 span length and downward, 2-WC model has higher magnitude than NC model. The shift of 2-WC streamwise and spanwise velocities caused the absolute angle and incidence angle for 2-WC in Fig. 9 to be shifted.

For tangential velocity, the deviation of 2-WC from NC takes effect close to hub. There is an increase of tangential velocity magnitude at hub due to the reduction of blade speed because of the smaller radius at leading edge. Thus, in order to maintain the flow rate, tangential velocity increases and this effect is more significant for 2-WC. At the shroud area, tangential velocity changes direction from negative to positive which causes the incidence angle to change in similar direction as well as shown in Fig. 9(b).

The results in this section shows that the non-uniform flow caused by the tongue greatly impact the velocity components and hence the absolute and incidence angle at the rotor inlet. Due to this non-uniformity as well, the effect of fluid-structure coupling is more visible at 0° compares to at 180° where the flow is more uniform.

### 3.3 Flow Characteristics at 10% Streamwise Plane

Flow characteristics at 10% streamwise of rotor blade were analyzed to evaluate the influence of rotor inlet flow close to the leading edge. Comparison of pressure contours and streamline plots for NC and 2-WC at 0° and 180° circumferential locations are presented in this section. Then velocity components at three spanwise positions at the 10% streamwise plane are also presented. Figure 11 depicts the location of the fluid passage at 0° and 180° circumferential location and also the position of 10% streamwise plane.
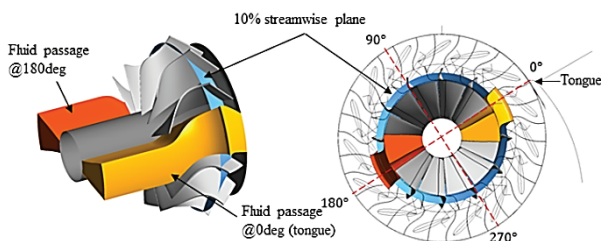


**Fig 11:** Fluid passage at 0° and 180° circumferential locations

Figure 12 shows comparison of pressure contours for NC and 2-WC models at 0° and 180° circumferential locations. The contours are displayed such that the view of the observer is facing the incoming flow at the leading edge toward the trailing edge. The black arrow in Fig. 12(a) shows the direction of rotor rotation which is in clockwise direction. The capital 'S' and 'P' represent suction surface and pressure surface respectively.

In general, the highest pressure area is at shroud close to pressure side and gradually decreases toward the hub and suction side. This high pressure area is greater at 180° compares to at 0°. Pressure decreases gradually at pressure side but has rapid change at suction side. In NC model for both locations, there is a localized low-pressure region at the leading edge suction side which is not visible in 2-WC model as shown in the red circles in Fig. 12. Among the pressure contours shown in Fig. 12, the maximum and minimum pressure recorded is at 0° circumferential location.
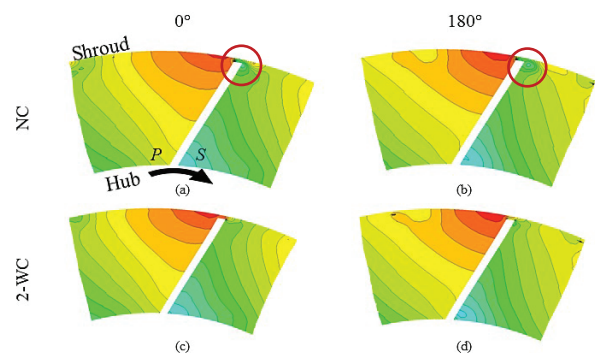


**Fig 12:** Comparison of pressure contours for NC and 2-WC models at 0° and 180° circumferential locations

Figure 13 shows comparison of streamlines plots for NC and 2-WC models at 0° and 180° circumferential locations at 10% streamwise plane. At each of the streamline plot, three spanwise positions were analyzed which were at 90%, 50% and 5% spanwise illustrated as black lines in Fig. 13(a). 90% and 5% spanwise were chosen because there were separation flows occurred and 50% spanwise was added for reference.
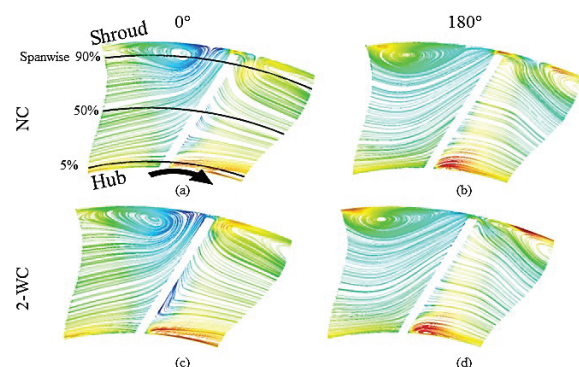


**Fig 13:** Comparison of streamlines plots for NC and 2-WC models at 0° and 180° circumferential locations.

In order to have detail conditions, the streamline plots where flow separation occurred were enlarged and accompanied with velocity components plots. Velocity

components are represented by meridional velocity, radial velocity and tangential velocity. Meridional velocity $v_m$ components can also be represented by radial velocity $v_r$ and axial velocity $v_a$ as shown in Eq. 11. This is the similar meridional velocity as shown in Eq. 10.

$$v_m = v_a + v_r \qquad (11)$$

Figure 14 shows the enlarged view of the streamline plots around 90% spanwise line at 10% streamwise plane. Figure 14(a) and 14(c) display the streamline plots at 0° location for NC and 2-WC model respectively which correlates with velocity plot in Fig. 15(a). Fig. 14(b) and (d) display the streamline plot at 180° location for NC and 2-WC model respectively which correlates with velocity plot in Fig. 15(b).
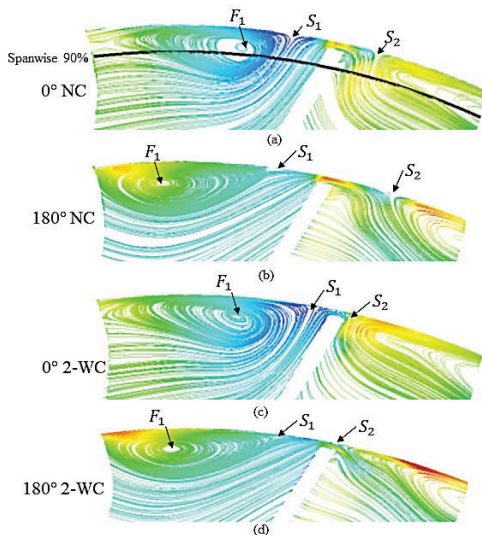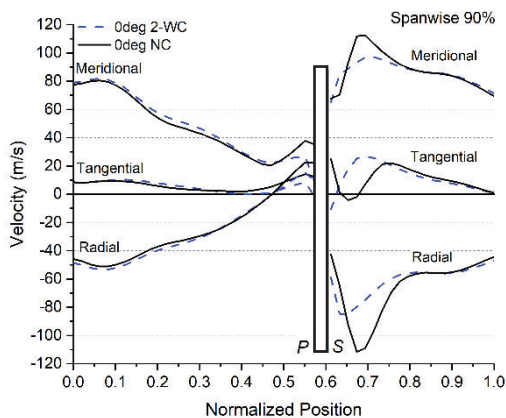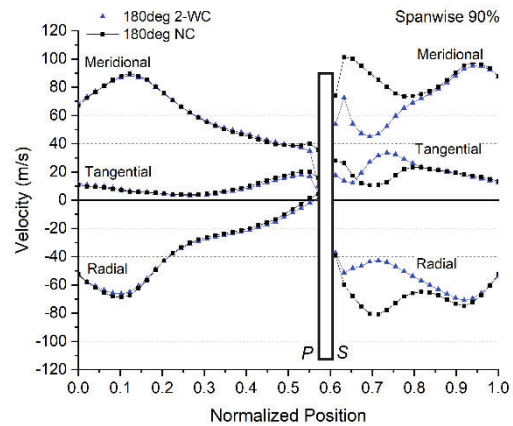


**Fig 14:** Enlarged view around 90% spanwise line at 10% streamwise plane



(a)   Velocity components 0° circumferential locations.



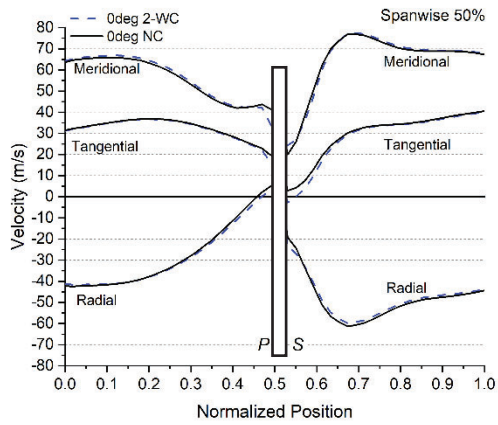(b)   Velocity components 180° circumferential locations.

**Fig 15:** Velocity components at 90% spanwise line

The meridional velocity continuously to drop from the mid-flow passage toward the pressure surface due to rotor blockage[31] and also the negative direction of radial velocity. Meridional velocity in Fig. 15(a) shows a drop at normalized position 0.47 which is at the vortex area. Meridional velocity at 180° shown in Fig. 15(b) shows similar trend of reduction but maintain higher value compare to 0° circumference location. The velocity components at pressure side at both locations show insignificant different between NC and 2-WC except at the pressure surface where 2-WC velocity components have lower magnitude.

Inside the tip clearance, the velocity in NC model is substantially higher compares to 2-WC model. This is due to the localized low-pressure region at the leading edge of the suction side as shown in Fig. 12(a) and (b) hence creating higher pressure difference. At suction side, the differences between NC and 2-WC are more significant. There is an appearance of second saddle point $S_2$ at suction side. Since only one critical point appears, there is no separation flow observed in this area. Due to high velocity exiting from the tip clearance in NC, the second saddle point $S_2$ is pushed farther away from the suction surface. Whereby in 2-WC, this saddle point is located close at the tip clearance exit. The second saddle point $S_2$ also splits the flow into two, one coming from the tip clearance and the other one from incoming flow from the rotor inlet. Comparing between 0° and 180° location in NC model, saddle point $S_2$ at 0° location appears closer to the suction surface which force the high velocity flow from the tip clearance to change direction abruptly and move radially downward. This is shown in Fig. 15(a) where the radial velocity for NC model has sudden increase in magnitude toward negative direction. The variation of the velocities between NC and 2-WC models take place from suction surface until 0.8 normalized position and after that they are in a good agreement. Tangential velocities on both pressure and suction sides are very low because of high

blade speed at higher spanwise position, thus maintaining the overall flow rate.

As observed in Fig. 13 at 50% spanwise, there is no separation or critical points appear at this region. Velocity components plots at 50% spanwise line are displayed in Fig. 16.



(a)  Velocity components 0° circumferential locations
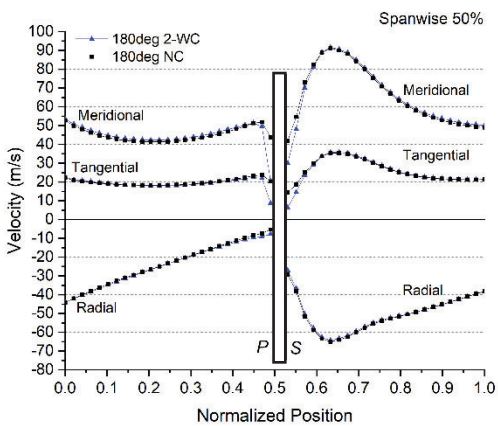


(b)  Velocity components 180° circumferential locations

**Fig 16:** Velocity components at 50% spanwise line

Figure 16(a) shows the comparison for NC and 2-WC at 0° circumferential location and Fig. 16 (b) is at 180° circumferential location. There is no significant difference between the two models except at suction and pressure surface which 2-WC model consistently show lower values. Tangential velocity is higher at this spanwise line compare to at 90% spanwise line as the blade speed reduces due to lower leading edge radius. Radial velocity remains the main component in meridional velocity. The velocity components at 0° circumferential location at pressure side exhibits different patterns compares to 180° circumferential location and with its meridional velocity has higher magnitude.

Figure 17 shows the enlarged view of Fig. 13 of the flow topology around 5% spanwise. Since NC and 2-WC models exhibit similar topologies, only NC model at 0° (Fig. 17(a)) and 180° (Fig. 17(b)) circumferential locations are shown in this figure.
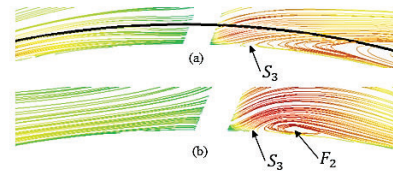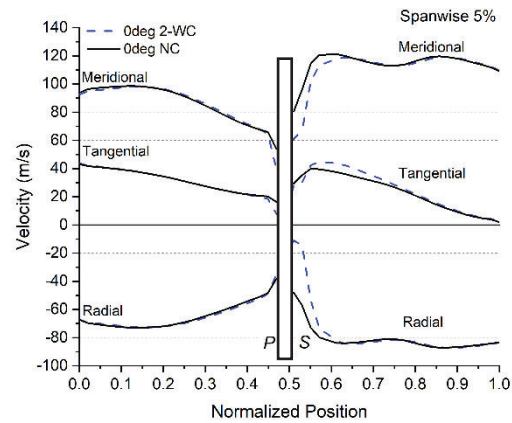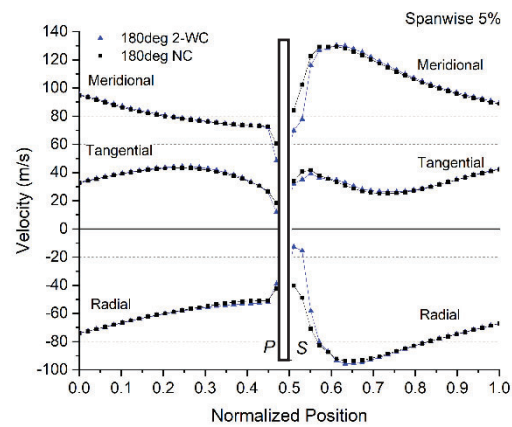


**Fig. 17:** Enlarged view around 5% spanwise line at 10% streamwise plane (a) 0° and (b) 180° circumferential locations.



(a)  Velocity components 0° circumferential locations



(b)  Velocity components 180° circumferential locations.

**Fig 18:** Velocity components at 5% spanwise line

As this region is at the lowest pressure region particularly at hub of suction side as shown in Fig. 12, the flow is drawn in with high acceleration There is a third saddle point $S_3$ appear in both locations. However, the second focus point $F_2$ only appears at 180° location. These two critical points cause localized tornado-like vortex at the hub close to suction surface. Similar observation was reported by D. Palfreyman and R.F. Martinez-Botaz[23] which occurred at 20% spanwise.

At pressure side as illustrated in Fig. 18, there is no significant different between NC and 2-WC except at the pressure surface. However, significant deviation occurs at

suction side from the suction surface until 0.57 normalized location. At that position, the lowest pressure different is recorded between NC and 2-WC which is 0.319%.

The results in this section shows the significant difference between NC and 2-WC occurs close to the shroud (90% spanwise) due to localized low-pressure region in NC. All three spanwise locations at 10% streamwise plane shows consistent different of velocity magnitude at pressure and suction surfaces of the blades between NC and 2-WC models.

### 3.4 Blade deformation and stress

Even though discussion on the structural performance is not within the scope of this paper, the results of the deformation and stress of the blades for NC and 2-WC are shown in order to complete the analysis covering the structure domain.
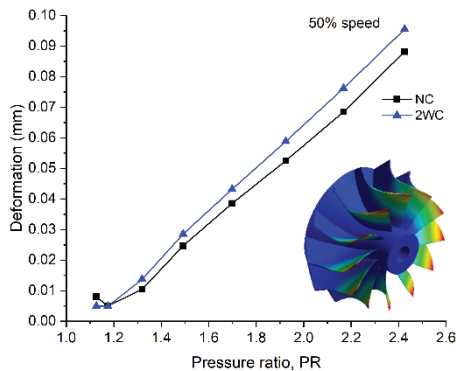


(a) Blade deformation
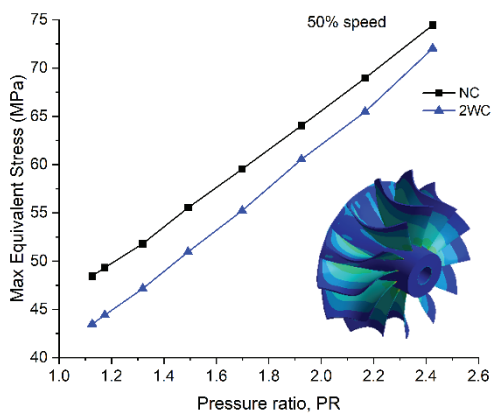


(b) Blade maximum equivalent stress

**Fig 19:** Comparison of blade structure performance for NC and 2-WC models

Figure 19(a) shows the deformation of the blades with its contour plot and Fig. 19(b) shows the maximum equivalent stress of the blades with its contour plot for NC and 2-WC for similar range of pressure ratio as in Fig. 5(a). 2-WC model shows lower deformation value because of the additional damping imposes by the fluid. The average difference of deformation of the blade relative to NC

model is 6.31% where the highest difference is at PR of 1.32.

The maximum equivalent stress shows that 2-WC model has lower value with average difference of 7.30%. The pattern of the deformation shown in Fig. 19 (a) is similar as reported by S. Netzhammer et al.[32] where the tip of the trailing edge experiences the largest deformation. This is because of its thin geometry thus having a lower stiffness. The stress pattern shown in Fig. 19(b) is similar as reported by S.Shan et al.[33] where the highest stress occurs at the root of the blade and the stress is radially distributed. This shows that the dominant force is centrifugal force with pulling effect toward center of rotation. However, both papers by S. Netzhammer et al.[32] and S.Shan et al.[33] were using RFT as these are the closest cases to be compared as data for MFT is not available. I. Ubolom[34] also did comparison of decoupled and coupled FSI analysis but for gas turbine. The analysis was conducted for unsteady condition to investigate the effect of FSI on stress and fatigue life of the turbine blade. The results reported show similar trend with the findings of this paper where the deformation or displacement of the blade is lower for coupled FSI model. It also concluded that the displacement has negligible influence on aerodynamic performance. However, the coupled FSI mean stress value in[34] shows a contradict trend with this paper. A. Ismaiel and S. Yoshida[35] highlighted that static loads might not be sufficient to evaluate the performance of the blades as in the actual condition, the blades experience cyclic loading, which this scope will be covered in the future paper.

## 4. Conclusions

This paper presents the analysis of flow characteristics of MFT rotor inlet by comparing two numerical models, non-coupled (NC) fluid-structure and two-way coupled (2-WC) fluid-structure interaction. Efficiency vs. velocity ratio shows that 2-WC numerical model has the closest efficiency value to the experimental data. However, the efficiency different between 2-WC and NC is very minimal by only 1.16%.

Flow analysis at the rotor inlet concludes that non-uniform flow caused by the volute tongue has great impact on the flow angle distribution along spanwise direction. There are differences for flow angle distributions between 2-WC and NC models at the tongue (0°) but not at 180° which possess more uniform flow. The influence of inlet flow angle distribution on rotor flow passage was analyzed at 10% streamwise plane at three circumference spanwise positions. The most significant difference at 10% streamwise plane is in NC model, where there is a localized low-pressure region at the leading edge of suction surface which cause very high velocity magnitude at the tip clearance. This leads to apparent differences in velocity component patterns at suction side between NC and 2-WC models. Overall, the velocity components for

NC and 2-WC models at pressure sides for all spanwise locations are almost identical except at the pressure surface of the blade. In suction side, the velocity components display certain variations between NC and 2-WC from suction surface to the mid flow passage due to the tip clearance flow and rapid pressure change. The consistent variation of all velocities on the pressure and suction surface of the blade between NC and 2-WC models are because of the ALE formulation which takes into account the mesh velocity of the fluid-structure interface.

On the structure side, blade deformation and maximum equivalent stress results are presented over similar range of pressure ratio. The results show that the average difference in blade deformation and maximum stress between NC and 2-WC models are 6.31% and 7.30% respectively.

This study is ongoing research of comparison between NC and 2-WC numerical models for flow characteristics inside MFT flow passage. Further analysis is required to have concrete findings on the comparison of these two numerical models, for example analysis at multiple different rotor speed and investigation at different locations covering multiple areas at streamwise, spanwise and blade-to-blade. Transient analysis with pulsating flow must also be considered as it represents the actual operating condition of the turbine.

Based on the results of this paper, it is concluded that if the study related to overall performance of turbine, a non-coupled simulation model is sufficient as the outcome will have minimal difference compared to coupled simulation. In addition, coupled simulation model is computationally expensive. However, if the study is specifically related to tongue area or structural performance, thus fully coupled simulation model should be considered for better accuracy.

## Acknowledgements

## Nomenclature

| | |
|---|---|
| $C$ | damping matrix (N m s$^{-1)}$ |
| $c_p$ | specific heat capacity (J kg$^{-1}$ K$^{-1}$) |
| $F$ | force matrix (N) |
| $K$ | stiffness matrix (N m$^{-1}$) |
| $M$ | mass matrix (kg) |
| $\dot{m}$ | mass flow rate (kg/s) |
| $N$ | turbine speed (rpm) |
| n | unit vector (-) |
| $p$ | pressure (Pa) |
| $T$ | temperature (K) |
| $t$ | time (s) |
| $u$ | mesh velocity (m s$^{-1}$) |
| $v$ | fluid velocity (m s$^{-1}$) |
| $W$ | power (W) |
| $x$ | displacement (m) |

*Greek symbols*

| | |
|---|---|
| $\eta$ | efficiency (-) |
| $\Gamma$ | interface (-) |
| $\gamma$ | specific heat ratio (-) |
| $\mu$ | dynamic viscosity (N s m$^{-2}$) |
| $\Omega$ | domain (-) |
| $\rho$ | density (kg m$^{-3}$) |
| $\sigma$ | stress (N m$^{-2}$) |
| $\tau$ | torque (N m) |

*Subscripts*

| | |
|---|---|
| $a$ | axial |
| $act$ | actual |
| $f$ | fluid |
| $fs$ | fluid-solid |
| $i, j$ | Cartesian direction |
| $in$ | inlet |
| $isen$ | isentropic |
| $m$ | meridional |
| $out$ | outlet |
| $r$ | radial |
| $s$ | solid |
| $st$ | streamwise |
| $st$ | spanwise |
| $t$ | turbine |
| $tg$ | tangential |

## References

1) IEA, "Key World Energy Statistics 2021," (2021).
2) S. Hori, "Implications of energy efficiency and

economic growth in developing countries." *Evergreen.*, 6 9-14 (2012).

3) S. Hori, and T. Fujita, "Incentive Mechanisms for the Development of a Low-carbon Society in Asia." *Evergreen.*, 1 24-28 (2010).

4) T. Fujisaki, "Evaluation of green paradox: case study of Japan." *Evergreen.*, 5(4) 26-31 (2018) doi.org/10.5109/2174855

5) EPA. "The 2020 EPA Automotive Trends Report." (2021).

6) M.H Padzillah, S. Rajoo, and R.F. Martinez-Botas, "Experimental And Numerical Investigation On Flow Angle Characteristics Of An Automotive Mixed Flow Turbocharger Turbine." *J. Tek.*, 77(8) 7-12 (2015).

7) R. Morrison, S. Spence, S. Kim, D. Filsinger, and T. Leonard, "Investigation of the effects of flow conditions at rotor inlet on mixed flow turbine performance for automotive applications" *Proceed. Int. Turbo. Sem, Tianjin, China.*, (2016).

8) T. Leonard, S. Spence, A. Starke, D. Filsinger, "Numerical and experimental investigation of the impact of mixed flow turbine inlet cone angle and inlet blade angle." *J. Turbo.*, 141(8) p. 081001 (2019).

9) S.P. Lee, S.M. Barrans, M.L. Jupp, and A.K. Nickson, "Investigation into the impact of span-wise flow distribution on the performance of a mixed flow turbine." *InTurbo Expo: Pow. Land, Sea, and Air ASME.*, 51005 p.V02BT44A027 (2018).

10) M.H. Padzillah, S. Rajoo, R.F. Martinez-Botas, "A Detailed Comparison on the Influence of Flow Unsteadiness Between the Vaned and Vaneless Mixed-Flow Turbocharger Turbine." *J. Eng. Gas Turb. Pow.*, 140(4) 042601 (2018).

11) D. Japikse and N. Baines, "*Introduction to Turbomachinery.*" Norwich, VT: Concepts Eti (1994).

12) R. Morrison, S. Spence, S.I Kim, T. Leonard, A. Starke A, "Evaluating the use of leaned stator vanes to produce a non-uniform flow distribution across the inlet span of a mixed flow turbine rotor." *J. Turbo.*, 142(12) p.121001 (2020).

13) Z. Ding, W. Zhuge, Y. Zhang, Y. Chen, C. Liu, "Investigation on Unsteady and Steady Swirling Inflow Effect on Turbocharger Turbine Performance." *InTurbo Expo: Pow. Land, Sea, and Air ASME.*, 58714, p.V008T26A016 (2019).

14) B. Gupta, T. Hoshi, S. Ogawa, M. Osako, H. Yoshizawa, N. Inoue. "Development of Next Generation Variable Geometry Turbocharger for Commercial Vehicles." *SAE.*, 0148-7191 (2021).

15) U. Khairuddin, A.W. Costall, R.F. Martinez-Botas, "Influence of Geometrical Parameters on Aerodynamic Optimization of a Mixed-Flow Turbocharger Turbine." *InTurbo Expo: Pow. Land, Sea, and Air ASME.*, 56659 p.V02CT42A002 (2015).

16) L. Chen, W. Zhuge, Y. Zhang, S. Zhang, "The effect of leading edge curvature on a mixed flow turbine performance under pulsating flow conditions". *InTurbo Expo: Pow. Land, Sea, and Air ASME.*, 48883, 1143-1149 (2009).

17) G. Hou, J. Wang, A. Layton, "Numerical methods for fluid-structure interaction—a review." *Comm. Comp. Phys.*, 12(2) 337-377 (2012).

18) M.H. Souli, D.J. Benson, "*Arbitrary Lagrangian Eulerian and fluid-structure interaction: numerical simulation.*" John Wiley & Sons, (2013).

19) S. Rajoo, "*Steady and pulsating performance of a variable geometry mixed flow turbocharger turbine.*" Diss. Department of Mechanical Engineering, Imperial College London, (2007).

20) M. Abidat, "*Design and testing of a highly loaded mixed flow turbine.*" Diss. University of London, (1991).

21) A. Ismaiel, and S. Yoshida, "Study of turbulence intensity effect on the fatigue lifetime of wind turbines." Evergreen., 5 (1) 25-32 (2018). doi.org/10.5109/1929727

22) ANSYS. "Turbulence Models." https://ansyshelp.ansys.com/ (accessed Aug 15, 2021).

23) D. Palfreyman, and R.F. Martinez-Botas, "Numerical Study of the Internal Flow Field Characteristics in Mixed Flow Turbines." *InTurbo Expo: Pow. Land, Sea, and Air ASME.*, 3610, 455-472 (2002).

24) P. Newton, R.F. Martinez-Botas, and M. Seiler, "A Three-Dimensional Computational Study of Pulsating Flow Inside a Double Entry Turbine." *J. Turb.*, 137(3) 031001-031001-031010 (2014).

25) Z.K. Omar, H. Mohammed, H.M. Kamel, "Computational Aerodynamic Performance Of Mixed-Flow Turbine Blade Design." *Eng. Rev.*, 37(2) 201-213 (2017).

26) S.P. Lee, M.L. Jupp, S.M. Barrans, and A.K. Nickson, "Analysis of leading edge flow characteristics in a mixed flow turbine under pulsating flows". *Proceed. Inst. Mech. Eng. Part A: J. Pow. Energy.*, 233(1) 78-95 (2019).

27) N. Watson, and M. Janota, "*Turbocharging the internal combustion engine.*" Macmillan International Higher Education (1982).

28) M.H. Padzillah, S. Rajoo, M. Yang, R.F. Martinez-Botas. "Influence of pulsating flow frequencies towards the flow angle distributions of an automotive turbocharger mixed-flow turbine." *Energy Conver. Mgmt.*, 98 449-462 (2015).

29) B. Yang, P. Newton, R.F. Martinez-Botas, "Understanding of Secondary Flows and Losses in Radial and Mixed Flow Turbines." *J. Turbo.*, 142(8) 081006 (2020).

30) M.H. Padzillah, S. Rajoo, R.F. Martinez-Botas, "Flow Field Analysis of an Automotive Mixed Flow Turbocharger Turbine." *J. Tek.* 77(8) 21-27 (2015).

31) N. Karamanis, R.F. Martinez-Botas, and C. Su. "Mixed flow turbines: Inlet and exit flow under steady and pulsating conditions". *InTurbo Expo: Pow.*

*Land, Sea, and Air ASME.,* 123(2), 359-371 (2001)

32) S. Netzhammer, D.M. Vogt, S. Kraetschmer, J. Leweux, and A. Koengeter, "Aerodynamic Excitation Analysis of Radial Turbine Blades due to Unsteady Flow From Vaneless Turbine Housings." *ASME Turb Exp: Turb. Tech. Conf. Expos.,* 50930 p. V07BT36A015 (2017).

33) S. Shan, A. Hou, X. Zheng, Z. Zhang, and M. Zhang, "Influence of the Aerodynamic Vibration Excitation on the Turbine Blade Vibration in a Vehicle Turbocharger." *ASME Int. Mech. Eng. Congr. Expo.,* 56437, p. V014T15A011 (2013).

34) I. Ubulom, "Influence of fluid-structure interaction modelling on the stress and fatigue life evaluation of a gas turbine blade." *Proceed. Inst. Mech. Eng. Part A: J. Pow. Energy.,* 235(5) 1019-1038 (2021).

35) A. Ismaiel, and S. Yoshida, "Fatigue Analysis of an Optimized HAWT Composite Blade." *Evergreen.,* 4 (2-3) 1-6 (2017). doi.org/10.5109/1929656